Received: 17 August 2021 | Revised: 2 November 2021 | Accepted: 13 November 2021

DOI: 10.1002/jbm.b.34971

RESEARCH ARTICLE

Controlling the bone regeneration properties of bioactive glass: Effect of particle shape and size

Mark Borden[1] | **Lance Erik Westerlund**[2] | **Vedran Lovric**[3] | **William Walsh**[3]

[1]Synergy Biomedical, Wayne, Pennsylvania, USA

[2]Hughston Spine, Hughston Clinic, Columbus, Georgia, USA

[3]Surgical and Orthopedic Research Laboratories, Prince of Wales Clinical School, UNSW Sydney, Sydney, New South Wales, Australia

Correspondence
Mark Borden, Synergy Biomedical, 565 E. Swedesford Rd., Suite 310, Wayne, PA 19087, USA.
Email: mborden@synergybiomedical.com

Abstract

The ability of particulate bioactive glass to function as an effective bone graft material is directly related to its *in vivo* dissolution, ion release, and interparticle spacing (area associated with bone in-growth). A spherical shape represents an optimal geometry to control bioactive glass bone formation properties. Spherical particles were fabricated from 45S5 bioactive glass with unimodal (90–180, 180–355, and 355–500 μm) and bimodal size ranges (180–355/355–500 and 90–180/355–500 μm). Particles were formed into bone graft putties and compared to a commercially available product composed of irregular 45S5 bioactive glass particles (32–710 μm). Scanning electron microscopy characterization of spherical particles showed a relatively uniform sphere shape and smooth surfaces. Irregular particles were characterized by random shapes with flat surfaces and sharp edges. X-ray fluorescence and X-ray diffraction indicated that the spheroidization process maintained the properties of 45S5 bioactive glass. Cross-sectional micro-computed tomography imaging of the putty samples demonstrated that smaller spheres and irregular particles resulted denser packing patterns compared to the larger spheres. Isolated particles were immersed in simulated body fluid for 14 days to measure silicon ion release and bioactivity. Inductively coupled plasma spectroscopy showed faster ion release from smaller particles due to increased surface area. Bioactivity characterization of 14-day simulated body fluid exposed particle surfaces showed the presence of a hydroxycarbanoapatite mineral layer (characteristic of 45S5 bioactive glass) on all bioactive glass particles. Results demonstrated that spherical particles maintained the properties of the starting 45S5 bioactive glass, and that particle shape and size directly affected short-term glass dissolution, ion release, and interparticle spacing.

KEYWORDS
bioactive glass, bioactivity, bone graft, ion release, particle size, spheres, 45S5 bioglass

1 | INTRODUCTION

In the surgical treatment of orthopedic trauma and joint degeneration requiring fusion, bone grafts are commonly used to regenerate bone in osseous voids or gaps associated with restoring skeletal length, alignment, and stability. Over the years, a variety of graft materials have been utilized for such spinal and orthopedic applications. The clinical success of these graft materials is often based on the material properties and their involvement in the bone formation response. The core property of various types of autogenic, allogenic, and synthetic bone graft materials is the osteoconductive ability to support bone formation on the surface of the material. Once implanted, the graft functions as a scaffold that spans the bone defect and allows the bone formation response to occur. Although this osteoconductive process is common amongst all graft materials, certain bone grafts have additional properties that can have further significant, positive influences on the bone regeneration process. These advanced bone graft materials play an active role in bone formation and can result in a faster and more robust healing response. One such class of materials, bioactive glass, has garnered significant interest from both researchers and surgeons due to its unique bone forming properties.

The original bioactive glass formula (45S5 Bioglass) was discovered by Hench and was specifically formulated as a bone graft material.[1] It is composed of 45% SiO_2, 24.5% CaO, 24.5% Na_2O, and 6% P_2O_5. Bioactive glass is biocompatible, resorbable, and possesses unique properties linked to its physiological dissolution. Once implanted and exposed to body fluid, the glass is eventually resorbed through a 6–9 month aqueous dissolution process. During this process, dissolution materials are released in a water-soluble, ionic form (calcium, phosphorus, silicon, and sodium ions). These ions are directly derived from the associated oxide components that form bioactive glass. This ion release property imparts bioactive glass with a particular set of characteristics and unique properties that are beneficial to the bone regeneration process.

Early in its discovery, Hench found that bioactive glass had the ability to form a calcium phosphate layer on its surface (*in vitro* and *in vivo*) and directly bond with bone.[2,3] This characteristic is called bioactivity and is the result of dissolution ions from the glass reacting with ions in body fluid. Following implantation, the preferential dissolution and release of calcium and sodium ions creates a silica-rich layer on the glass surface.[2] This serves as a nucleation site for the precipitation of a bone-like mineral material called hydroxycarbanoapatite (HCA).[4-6] The precipitated HCA is unique due to the presence of carbonate substitution within the apatite mineral. This differs from pure calcium phosphate materials commonly used as bone grafts (hydroxyapatite—HA; tricalcium phosphate—TCP) that lack carbonate substitution. *In vivo* testing has shown that, once the bioactive layer is created, it provides an optimal surface for bone formation that results in a chemical bond between the glass and the new bone.[6,7] Testing has also shown that HCA is advantageous over HA and TCP due to a shortened cellular preparation phase at the beginning of the bone formation response.[8,9] Although bioactivity was regarded as the primary mechanism for the observed positive effects of bioactive glass into the early 1990's, it was an incomplete understanding of the bioactive glass healing response.

In this respect, the initial theory on why bioactive glass was an effective bone graft material began to expand and evolve as new data emerged. Wilson et al. postulated that the increased bone formation response seen in various bioactive glass *in vivo* bone formation studies was due to the interaction of the dissolution ions with local cells.[10] Initially termed "osteoproduction", this concept was eventually confirmed through a number of *in vitro* and *in vivo* studies, and become known as "osteostimulation".[11-15] These important studies found that bioactive glass dissolution ions, that were responsible for the formation of the bioactive layer, were also directly able to stimulate localized cells involved in the bone regeneration response. Exposure of osteoblasts to these ions resulted in an increase in cellular proliferation, protein expression, and mineralization. It was also found that these same dissolution ions caused the differentiation of bone marrow stem cells into osteoblasts[16-18] and had positive effects on angiogenesis.[19-21] These findings represented a pivotal discovery since similar cellular effects had previously only been associated with bone-derived growth factor proteins.

By the early 2000's, the new recognition of the osteostimulation characteristics and wider availability of bioactive glass products in more "surgeon-friendly" forms led to a significant increase in its use in surgery. Initially, bioactive glass was used as a surgical graft in a particulate form, but this was primarily limited to dental applications. In this application, the irregular shaped particles of bioactive glass (typically 90–710 μm) were specifically sized to provide some bulk cohesion when mixed with saline.[10,22] This was done to aid in the intraoperative handling and placement of the wet particles into small, contained dental defects. However, use in larger scale orthopedic and spine bone graft applications did not accelerate until the material was provided in forms designed to improve intraoperative handling and graft containment. This included putty forms (bioactive glass particles mixed with a moldable, resorbable carrier), and sheet forms (particles embedded in a porous collagen sheet). Although bioactive glass bone grafts have become increasingly popular and shown to be consistently clinically effective, nearly all current products continue to use the original, irregular geometric form of the glass that was designed for dental void filling (irregular particles in the 90–710 μm range). Since this basic particle design was identified prior to the studies showing the importance of bioactive glass ion release and osteostimulatory effects, the particle shape and size were never optimized to purposefully capitalize on the primary osteostimulatory properties of bioactive glass (while maintaining the advantages of tandem baseline bioactivity).

Based on the direct impact that bioactive glass dissolution ions have on bioactivity and osteostimulation, optimization of the particle shape and size may lead to an improved biological response to the glass. Since the bioactive glass dissolution process is an aqueous-based, surface effect, the most uniform shape to control ion release is a spherical particle with an equal diffusion distance from the center of the sphere. Additionally, the particle shape and size directly impact interparticle spacing and the associated area to support bone ingrowth. Therefore, by using a spherical shape and optimizing particle

size(s), the dissolution, ion release, and particle spacing can be precisely engineered to control the advanced properties of bioactive glass. Based on these relationships, this study is focused on the preliminary investigation into the effects of bioactive glass sphere shape and size on the physical and chemical properties of the material.

2 | MATERIALS AND METHODS

2.1 | Bioactive glass spheres

Bioactive glass with a 45S5 composition (45% SiO_2, 24.5% CaO, 24.5% Na_2O, 6% P_2O_5) and various spherical particles sizes was obtained from Mo-Sci Corporation (Rolla, MO). Bioactive glass spheres were manufactured using a flame spheroidization process. Resulting bioactive glass spheres were mechanically sieved into various unimodal size groups: 90–180 μm (Group 1), 180–355 μm (Group 2), and 355–500 μm (Group 3). Additional bimodal groups were created by weighing specific sized spheres in two ratios: 10% 90–180 μm and 90% 355–500 μm (Group 4), and 50% 180–355 μm and 50% 355–500 μm (Group 5). A comparative bimodal group (Group 6) consisted of irregular bioactive glass particles (32–125; 90–710 μm; ratio not published) that were isolated from a commercially available bioactive glass bone graft product (Novabone Putty [Novabone Products, Alachua, FL]). The experimental groups are summarized in Table 1.

2.2 | Bone graft putties

Bone graft putties were created by combining 45S5 bioactive glass spheres with a moldable carrier. Spherical bioactive glass putties were manufactured by Synergy Biomedical (Wayne, PA) and were based on the commercially available BioSphere Putty product. Putties were prepared by combining various sized 45S5 bioactive glass spheres (80% w/w) with a phospholipid carrier (20% w/w). The phospholipid carrier consisted of a 65%:35% mixture of Phosal 53 MCT and Phospholipon 90G (Phospholipoid GmBh). Putty samples were gamma sterilized prior to testing. An irregular particle bioactive glass putty with a bimodal size range (32–125/90–710 μm) was also evaluated (Novabone Putty, Novabone LLC). According to the manufacturer, Novabone Putty is composed of 69% (w/w) 45S5 bioactive glass particles mixed with a polyethylene glycol/glycerol carrier (31% w/w). The product is also gamma sterilized.

TABLE 1 Summary of the various bioactive glass particle shapes and sizes

Group	Particle shape	Size (μm)
1	Sphere	90–180
2	Sphere	180–355
3	Sphere	355–500
4	Sphere	10% 90–180 90% 355–500
5	Sphere	50% 180–355 50% 355–500
6	Irregular	32–125 90–710

2.3 | Micro-computed tomography—putty characterization

Three cross-sectional micro-computed tomography (microCT) images (Inveon microCT System, Siemens Inc.) were taken of the putty samples within their product syringes to evaluate cross-section particle packing. Inter-particle spacing was assessed by image analysis software (Matlab, Mathworks, Inc). Images from each sample were thresholded using Image J (National Institute of Health) and were analyzed for inter-particle spacing area with MatLab. Percent area was calculated from the inter-particle area and the overall area of the putty sample cross-section.

2.4 | Bioactive glass particle separation

Certain analytical tests conducted on the putties required bioactive glass particles to be isolated from their associated carrier. This was accomplished by dissolving the carriers with a solvent (methylene chloride—VWR Scientific). Samples were placed in an excess amount of solvent and broken apart. Fresh solvent was added, and the samples were agitated until the bioactive glass was freely flowing. Particles were further rinsed with solvent to completely remove the residual carrier and air-dried.

2.5 | Particle characterization

Particles isolated from the bioactive glass putties were subjected to a variety of analytical methods. Testing was conducted to evaluate the effect of spheroidization process on the physical and chemical properties of the glass and to confirm it retained its 45S5 composition. Standard, irregular shaped 45S5 bioactive glass particles isolated from Novabone Putty were used as a control.

2.5.1 | Scanning electron microscopy

Sphere morphology was visualized using a scanning electron microscope (Hitachi TM 1000, Hitachi Inc.). Particles were affixed to an scanning electron microscopy (SEM) stage and gold coated. Images were taken at a 250X magnification to visualize overall particle morphology.

2.5.2 | Particle size analysis

Particle size analysis ($n = 3$ samples per group) was conducted using laser scattering particle size analyzer (Mastersizer S, Malvern Pananalytical, Ltd). Particle size distribution was measured.

2.5.3 | X-ray fluorescence spectroscopy

Bioactive glass chemical composition ($n = 3$ samples per group) was conducted using a sequential wavelength dispersive X-ray fluorescence (WDXRF) spectrometer (Panalytical PW2400, Malvern Pananalytical, Ltd). Average weight % of the various oxide components was reported.

2.5.4 | X-ray diffraction

Bioactive glass crystallinity ($n = 3$ samples per group) was measured using an advanced simultaneous WDXRF spectrometer (Panalytical AXIOS, Malvern Pananalytical, Ltd). Diffractograms were generated from the data.

2.6 | Silicon ion release and bioactivity characterization

Bioactive glass particle isolated from the various putties were also evaluated according to in an *in vitro* dissolution model based on the method of Ducheyne.[23] Simulated body fluid (SBF) was created with Ducheyne's TES-10 formula consisting of 0.05 M tris hydroxymethyl aminomethane/HCl (Sigma) with additional plasma electrolytes and 10% newborn bovine serum. The SBF composition is shown in Table 2.

2.6.1 | Simulated body fluid immersion

Three samples (0.25 g each) from each group were placed in 250 ml of 37°C SBF buffer. The samples were incubated at 37°C for 14-days. At 1, 3, 4, 5, 6, 7, 9, 11, 12, and 14 days, the SBF solution from each sample was completely removed and saved for ICP analysis to determine the amount of silicon released from the bioactive glass particles. Fresh SBF solution pre-heated to 37°C was added to the sample containers to continue the 14-day dissolution. At the conclusion of the 14-day study, the particles from the associated samples were isolated from the immersion solution, rinsed with de-ionized water, and allowed to dry. The particles were then subjected to a bioactivity characterization.

TABLE 2 Simulated body fluid buffer composition used in the ion release and bioactivity testing

Simulated body fluid buffer	
0.05 M Trizma hydrochloride buffer	27.0 mM HCO_3
152.0 mM Na	1.5 mM Mg
135.0 mM Cl	0.4 mM SO_4
5.0 mM K	1.0 mM of H_2PO_4
2.5 mM Ca	10% Fetal bovine serum

2.6.2 | Silicon ion release

Interim SBF solution changes and the final 14-day solution ($n = 3$ samples per group) were analyzed by inductively coupled plasma atomic emission spectroscopy (ICP) (Avio Max, PerkinElmer Inc) to measure silicon ion concentration. Average silicon content (in mg) was calculated for each time point and cumulative silicone release was calculated. Data was used to generate a cumulative silicon content versus time release profile curve. Ion release data was analyzed using analysis of variance with post hoc (Games-Howell) pair-wise comparisons to determine any statistical differences between groups at each time point. A Levene test ($p = 0.05$) was used to confirm variance of homogeneity of the populations. Differences were considered significant at $p < 0.05$. Statistical analysis was performed using SPSS version 26.0 (SPSS Inc).

2.6.3 | Bioactivity characterization

Following the 14-day SBF exposure, isolated particles were subjected to surface characterization to evaluate the formation of a bioactive layer. A portion of the SBF-exposed particles ($n = 3$ samples/group) was characterized by scanning electron microscope–energy dispersive X-ray analysis (SEM–EDX). Particles were visualized by SEM imaging (250X and 1000X magnification) and surface elemental composition was determined by EDX analysis. A Hitachi TM 1000 Microscope was used for both analyses. A separate portion of the SBF-exposed particles ($n = 3$ samples per group) was analyzed using Fourier transform infrared spectrophotometry with an attenuated total reflectance probe (FTIR-ATR) (Spotlight 400 FTIR-ATR, Perkin Elmer Inc.).

3 | RESULTS

3.1 | Putty characterization—micro-computed tomography imaging

MicroCT imaging was used to examine the packing of the bioactive glass particles within the putty samples. Putty filled syringes were scanned and cross-sectional images were obtained. Due to the radiopacity of the bioactive glass and radiolucency of the carrier, the microCT images were able to clearly differentiate the particles from the carrier. Representative cross-sectional images of each group are shown in Figure 1. The microCT images show the bioactive glass particles (grey) arranged in packing patterns that varied with particle size and shape. The black area in between the particles represents the radiolucent carrier area. MicroCT imaging of the spherical particle putty samples showed that some of the particles contain empty bubbles within the spheres. This was an artifact from the sphere manufacturing process. The irregular particles, on the other hand, were seen as solid pieces of irregular shaped bioactive glass material. Qualitatively, the apparent packing density (number of particles/area) appeared to be correlated to particle size. The smallest particles (90–180 μm) had the highest packing density compared to the other

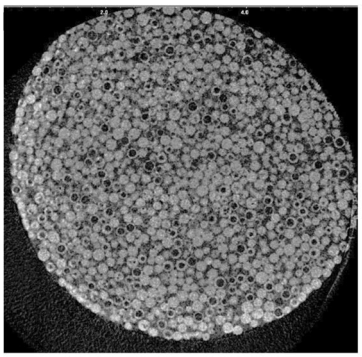

90-180um spherical particle putty

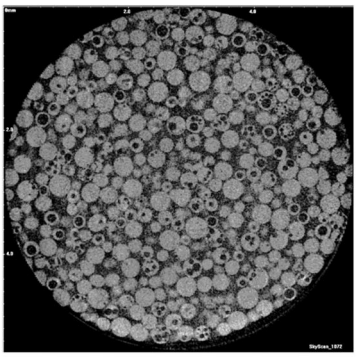

180-355um spherical particle putty

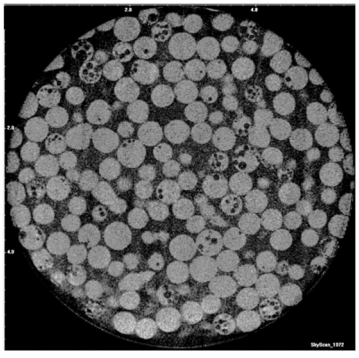

355-500um spherical particle putty

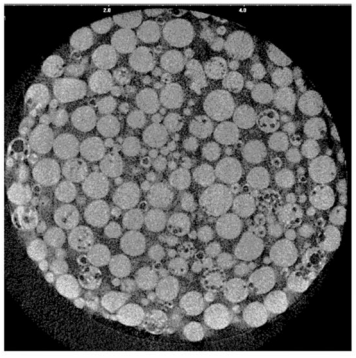

90-180/355-500um spherical particle putty

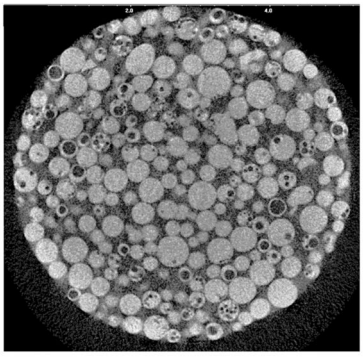

180-355/355-500um spherical particle putty

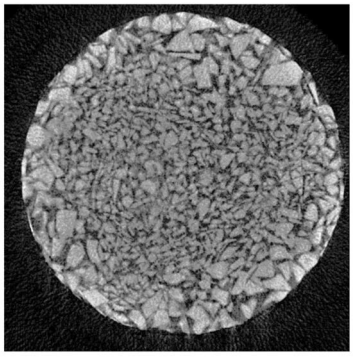

32-125/90-700um irregular particle putty

FIGURE 1 Cross-sectional micro-computed tomography imaging was used to visualize bioactive glass particle spacing in various putties packaged in open bore syringes

groups. Additionally, there appeared to be more spacing between the particles (inter-particle porosity) in the sphere-based groups compared to the irregular particles in the irregular particle group. This was confirmed by the image analysis, which showed the average percent carrier area of 32%–35% in the sphere groups and 26% in the irregular particle group. It was also observed that large particles in the irregular particle putty also tended to be localized on the outer circumference of the putty syringe. Conversely, the spherical particle groups showed a uniform and randomized distribution of particle sizes.

3.2 | Scanning electron microscopy imaging—isolated particles

Particle morphology was assessed via SEM imaging. Images of the various bioactive glass particles showed a distinct difference in particle morphology and size. A summary of representative SEM images is shown in Figure 2. The SEM images of the spherical glass showed that the particles had the expected spherical shape with occasional ellipsoid shapes. This corroborated the particle shape seen in the microCT cross-section imaging. In the SEM images, the spherical particles were uniform and matched their corresponding size range isolated by sieving. Images showed that the surface of the spherical particles was smooth and contained few small holes that were artifacts from the spheroidization process. The SEM images of the irregular particulate showed rough edged, shard-like particles with a non-uniform geometry. The particles varied broadly in shape and size and were characterized by flat surfaces with sharp, fractured edges.

3.3 | Particle size analysis

Laser scattering size analysis of the isolated particle showed expected differences in the particles size distribution curves for each group.

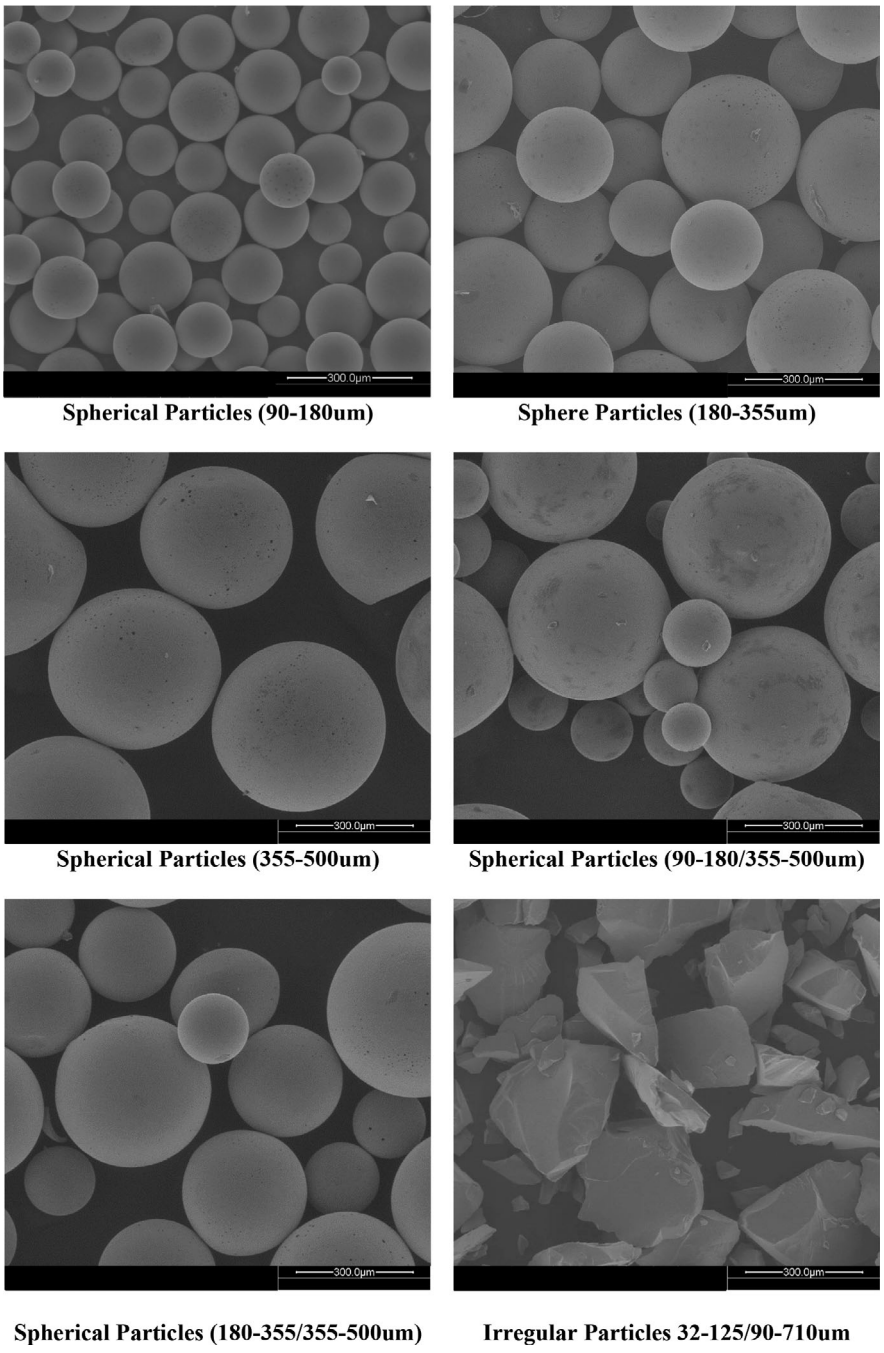

FIGURE 2 Scanning electron microscopy images of various bioactive glass particle shapes and sizes (250× magnification)

This is shown in Figure 3. The graph shows an expected shift in particle size distribution with increasing particle size. For the unimodal groups sphere groups, the 90–180 μm group had a peak centered at approximately 167 μm with a maximum average volume % of 33%. The 180–355 μm peak was centered at 267 μm (max. avg. volume 28%) and the 355–500 μm peak was centered at 443 μm (max. avg. volume 29%). For the bimodal groups, the 90–180/355–500 μm spherical particle group showed a distribution approximately centered at 424 μm (max. avg. volume 28%). In this group, the presence of the small 10% portion of 90–180 μm spheres is seen as a small shoulder on lower end of the distribution profile. For the 180–355/355–500 μm sphere group, the distribution peak was centered at 357 μm (max. avg. volume 25%). Since equal portions of these size ranges were included (50:50 mix of 180–355 and 355–500 μm), this group did not show a bimodal shoulder. In the irregular particle group (32–125/90–700 μm), the distribution curve was centered at 410 μm and had a distinctly different appearance than the sphere groups. The curve was very broad and had a much lower maximum average volume % (11%). This was attributed to the inclusion of more small-sized particles (32–125 μm).

3.4 | X-ray fluorescence and X-ray diffraction compositional analysis

Particles isolated from the various putties were also subjected to X-ray fluorescence (XRF) and X-ray diffraction (XRD) compositional analyses. This was conducted to evaluate whether the spheroidization, putty manufacturing, or gamma sterilization processes impacted the 45S5 bioactive glass composition. XRF analysis measured the oxide composition of isolated particles from each groups. Data was compared to the known composition for 45S5 bioactive glass. The results from the XRF testing are shown in Table 3. The results showed that the average chemical composition in all groups was similar to and matched the known composition for 45S5 bioactive glass. Oxide compositions were additionally within the manufacturing tolerances for 45S5 glass (Mo-Sci, Corp).

Isolated particles from each of the putties were additionally analyzed by XRD. A summary of the various XRD diffractograms is shown in Figure 4. Diffractograms for the various particle groups were similar and showed the characteristic 45S5 bioactive glass peak between 30° and 35°. Experimental diffractograms matched a known XRD diffractogram for 45S5 bioactive glass.[24] In addition, crystallinity analysis showed that all glass particles were 100% amorphous with no crystalline regions.

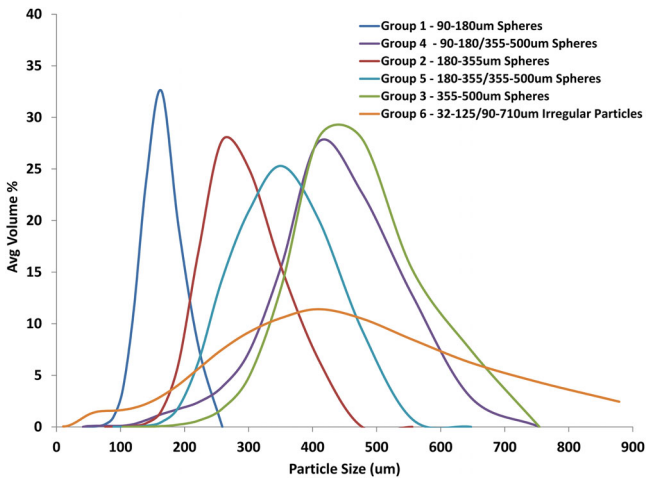

FIGURE 3 Laser scattering particle size distribution curves showing average %volume of various sized bioactive glass particles

3.5 | Silicon ion release and bioactivity characterization

Particles isolated from the various putty groups were exposed to SBF for a 14-day duration. A uniform sample size (250 mg) and SBF volume (250 ml) were used. Since silicon (Si) is not present in SBF, measurement of silicon in the SBF solutions allowed for characterization of bioactive glass dissolution. The release data was used to calculate average silicon ion amounts and cumulative amounts released over time. Silicon data from the SBF exposure period was analyzed in detail during the first 24-h, and over the course of 14-day study. During the initial 24-h immersion (Figure 5), all groups showed a burst effect for the first 10-h, indicated by a rapid increase in silicon concentration. At the 10-h time point, the irregular bioactive glass particles (32–710 μm) isolated from Novabone Putty (Group 6) showed the highest average concentration of silicon (9.2 mg) with the largest spherical particle groups (355–500 μm) showing the lowest released silicon (2.2 mg). Statistical analysis on the 10 h data, showed that the 32–710 μm irregular particles (Group 6) were significantly different ($p < 0.05$) than Group 2 (180–355 μm spheres), Group 3 (355–500 μm spheres), Group 4 (90–180/355–500 μm spheres), and Group 5 (180–355/355–500 μm spheres). There was no statistical difference ($p > 0.05$) between the irregular particles and the smallest 90–180 μm sphere group (Group 1). At end of the 24–h period, the 32–710 irregular particles in Group 6 continued to show the most released silicon (13.1 mg). Similar to the 10–h data, statistical analysis showed that this was significantly different ($p < 0.05$) than Groups 2, 3, 4, and 5. Within the unimodal sphere groups, the total amount of released silicon was found to increase as particle size decreased. The three unimodal spheres sizes showed 24–h average release amounts of 4.1 mg (Group 3:355–500 μm spheres), 7.0 mg (Group 2:180–355 μm spheres), and 11.0 mg (Group 1:90–180 μm spheres). Statistical analysis showed that the 355–500 μm group was statistically different ($p < 0.05$) than the 180–355 and 90–180 μm groups. This was expected due to the increase in surface area and resultant solubility of the smaller particles. The two bimodal sphere size ranges showed 24–h average silicon amounts of 6.4 mg (Group 5:90–180/355–500 μm) and 5.8 mg (Group 4:180–355/355–500 μm). As seen from the curves, these amounts fell between the release profiles of the Group2 180–355 μm spheres and the slow-release Group 3 (355–500 μm spheres).

Groups	SiO_2 (%)	CaO (%)	Na_2O (%)	P_2O_5 (%)
Group 1–90–180 μm spheres	45.8	24.3	24.0	6.0
Group 2–180–355 μm spheres	45.6	24.1	25.2	6.3
Group 3–355–500 μm spheres	44.9	24.0	25.1	6.2
Group 4–90–180/355–500 μm	45.0	24.5	25.6	6.2
Group 5–180–355/355–500 μm spheres	46.0	23.7	24.6	6.1
Group 6–32–125/90–710 μm irregular particles	45.3	24.4	24.1	6.4
Established 45S5 bioactive glass composition	45.0	24.5	24.5	6.0

TABLE 3 Average oxide content (X-ray fluorescence) of isolated bioactive glass particles compared to the known 45S5 bioactive glass composition

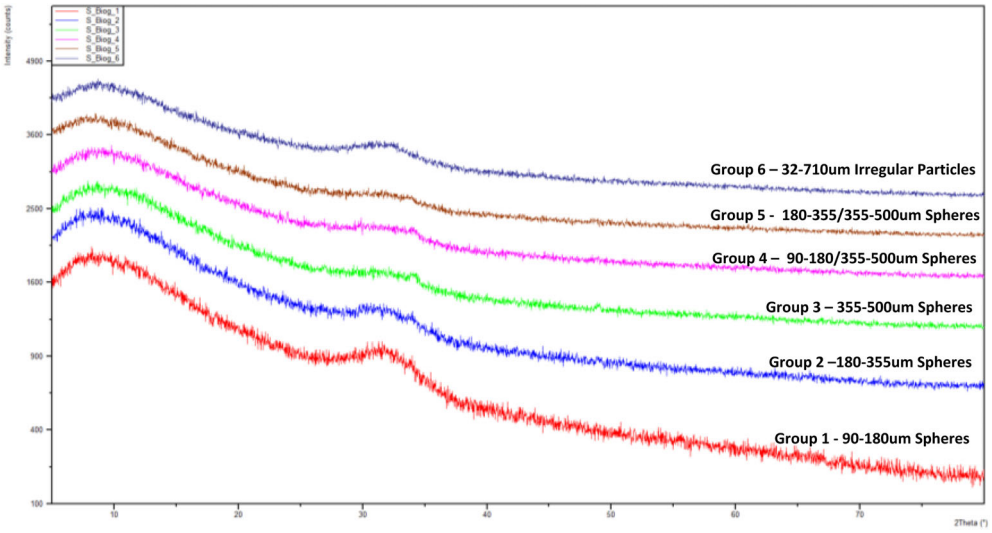

FIGURE 4 X-ray diffraction diffractograms for the various 45S5 particles showing similar patterns and 100% amorphous crystallinity

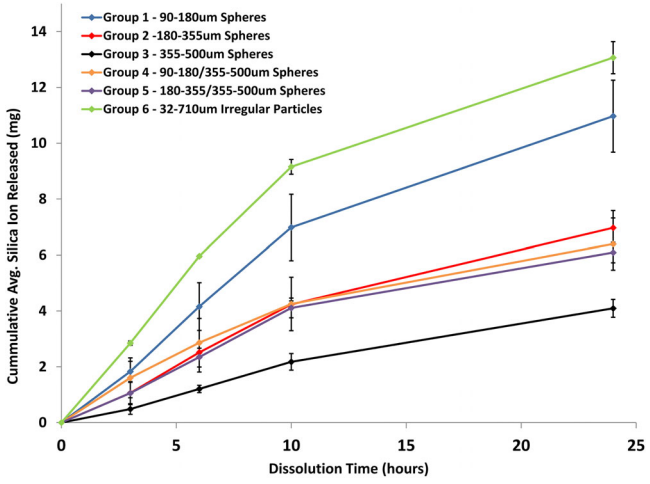

FIGURE 5 24-h silicon release amounts from the various bioactive glass particles exposed to simulated body fluid (SD error bars shown)

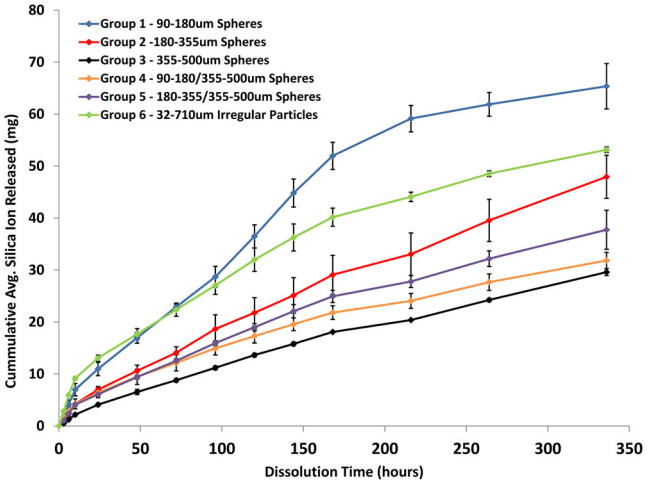

FIGURE 6 Complete silicon release amounts from the various bioactive glass particles exposed to simulated body fluid for a total of 336-h (SD error bars shown)

The full 14-day (336-h) release data from the SBF study is shown in Figure 6. The data showed dissolution profiles for Groups 2–6 that were consistent throughout the course of the study. The only exception was the 90–180 μm spheres (Group 1) which showed an increased dissolution rate from 100 to 168-h that surpassed the 32–710 μm irregular particles (Group 6). With a total average release of 65.4 mg, the 90–180 μm spheres were statistically different ($p < 0.05$) than all sphere groups (Group 2–5). However, there was no statistical difference ($p > 0.05$) between Group 1 and Group 6 (32–710 μm irregular particles). Similar to the 24-h data, the effect of particle size on release was still seen in the full 336-h data. In the unimodal spherical groups, the 90–180 μm spheres (Group 1) had the highest amount of total average released silicon (65.4 mg) at 336-h followed by the 180–355 μm spheres (49.5 mg; Group 2), and the 355–500 μm spheres (30.9 mg; Group 3). Group 1 was found to be significantly different ($p < 0.05$) than Groups 2 and 3. The two bimodal sphere groups also mimicked the 24-h data and remained in between the 180–355 and 355–500 μm groups with a 336-h release of 32.7 mg for the 90–180/355–500 μm spheres (Group 4) and 40.1 mg for the 180–355/355–500 μm spheres (Group 5). Although the 32–710 μm irregular particles (Group 6) were eventually surpassed by the 90–180 μm spheres (Group 1) at 100 -h, the irregular particles still showed a relatively fast release with a 336-h total amount of 55.5 mg. This was the second highest total below the 90–180 μm spheres (65.4 mg) and was found to be statistically different ($p < 0.05$) than the 355–500 μm spheres (Group 3) and 90–180/355–500 μm spheres (Group 4).

3.5.1 | Bioactivity characterization

At the conclusion of the 14-day SBF exposure, the particles were isolated to evaluate the formation of a bioactive HCA layer. Particles

from each sample were analyzed by SEM–EDX and FTIR to examine the compositional change to the bioactive glass particle surface. SEM imaging of the particle surface showed a similar response in all groups and appeared to be independent of particle shape or size. Representative images of the pre- and post-dissolution particles of a spherical particle group (Group 4: 90–180/355–500 μm) compared to the irregular particle group is shown in Figure 7. The SEM images showed that the 14-day exposure resulted in cracking in all of the bioactive glass particle groups due to the glass dissolution process. The surface of the particles appeared rougher with some flaking of the bioactive layer in the spherical groups. At the higher magnification (1000×) nodule formation was present. This indicated the presence of the bioactive layer. EDX analysis of the particle surfaces also showed a similar response in all the groups. Representative spectra from one of the groups (Group 4: 90–180/355–500 μm spheres) before and after 14 days of SBF immersion is shown in Figure 8. The pre-exposure EDX spectrum shows a prominent silicon peak, a moderately sized calcium peak, and a minor phosphorus peak. This is in line with the composition of bioactive glass (45% SiO_2, 24.5% CaO, 24.5% Na_2O, and 6% P_2O_5). In the post-dissolution spectrum, the presence of the bioactive layer was very evident. This was seen with an increase in intensity of the calcium and phosphorus peaks, and the complete absence of the silicon peak. This indicated a complete coating of the outer surface of the particles by the HCA layer. A similar response was also seen for the irregular particles (Group 6: 32–125/90–710 μm). In these samples, the pre-dissolution spectra showed Si peaks that disappeared following SBF exposure. Calcium and phosphorus peaks also increased following SBF exposure. Comparatively, the spectra were nearly identical for both the spherical and irregular particles. This confirmed the ability of the spherical particles to exhibit the same bioactive response as the irregular particles.

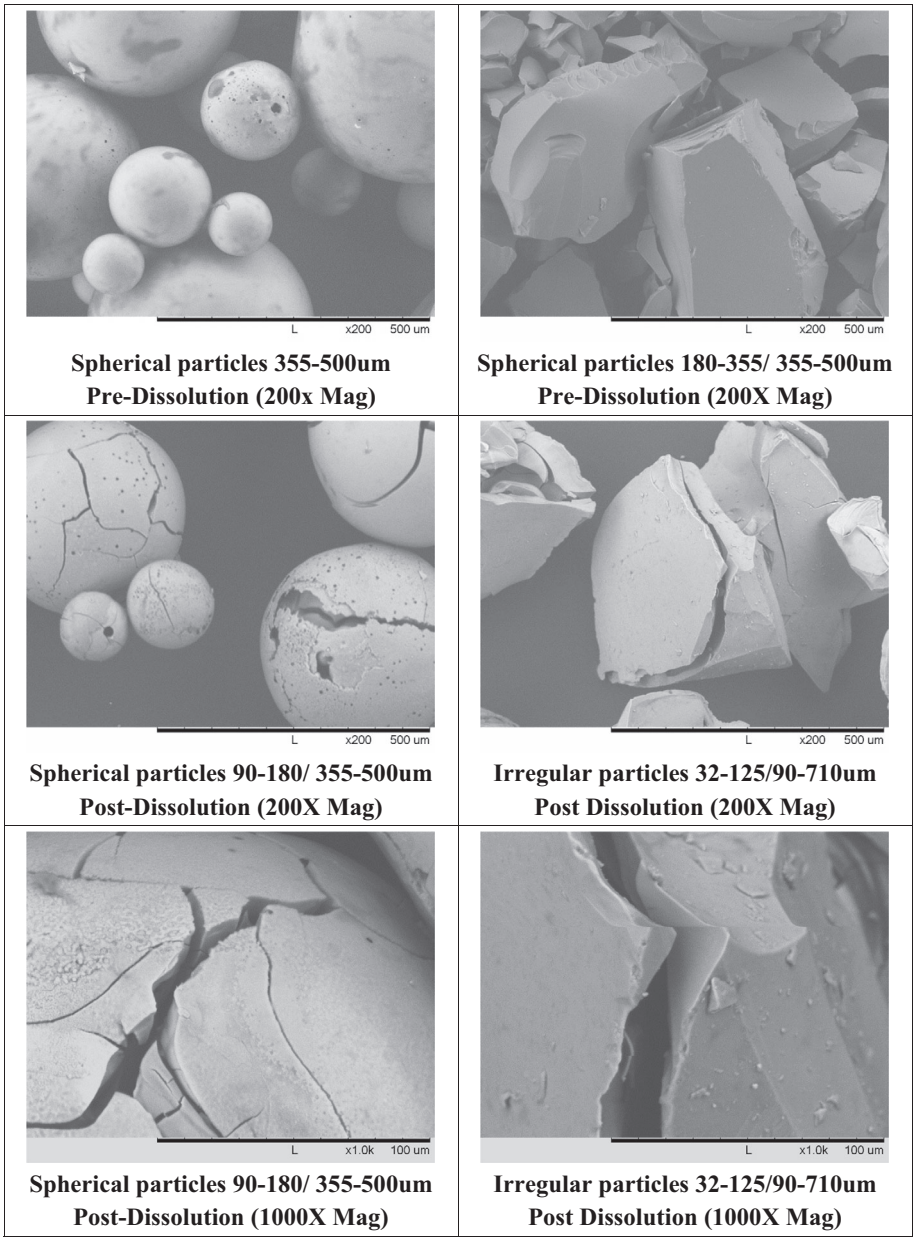

FIGURE 7 Representative scanning electron microscopy images (250X and 1000X) of 90–180/355–500 μm bioactive glass spheres (Group 4) and 32–710 μm irregular particles (Group 6) pre- and post-simulated body fluid dissolution (14-days)

3.5.2 | Fourier transform infrared

In addition to SEM–EDX, FTIR analysis was conducted on particles before and after exposure SBF to further characterize the bioactive layer. Results were identical between groups and confirmed that a bioactive layer formed and consisted of carbonated apatite (HCA). Representative spectra of one of the spherical groups (Group 4: 90–180/355–500 μm) before and after SBF exposure is found in Figure 9. The pre-exposure FTIR spectrum of the spherical particles (90–180/355–500 μm) showed the broad stretch of the Si—O—Si band between 770–1120 cm^{-1} which is characteristic of silica based bioactive glasses.[25,26] In the post-SBF exposure spectrum, the Si—O—Si peak is replaced by a strong phosphate (P—O) peak at (~1000 cm^{-1}). Additionally, carbonate (C—O) was present with peaks at ~1400 cm^{-1} and 1600 cm^{-1}. These peaks were representative of carbonate substitution into hydroxyapatite and confirmed the HCA composition of the bioactive layer.[27] The pre- and post-dissolution spectra for the irregular particles and other spherical particles sizes was identical to Figure 9 and also showed a broad Si—O—Si peak on the pre-exposure spectra that disappeared in the post-exposure spectra. The post-exposure spectra on these samples also showed phosphate (~1000 cm^{-1}) and carbonate peaks (1400 and 1600 cm^{-1}) characteristic of HCA. The FTIR data confirmed that all bioactive glass samples were able to form HCA on the material surface following SBF exposure.

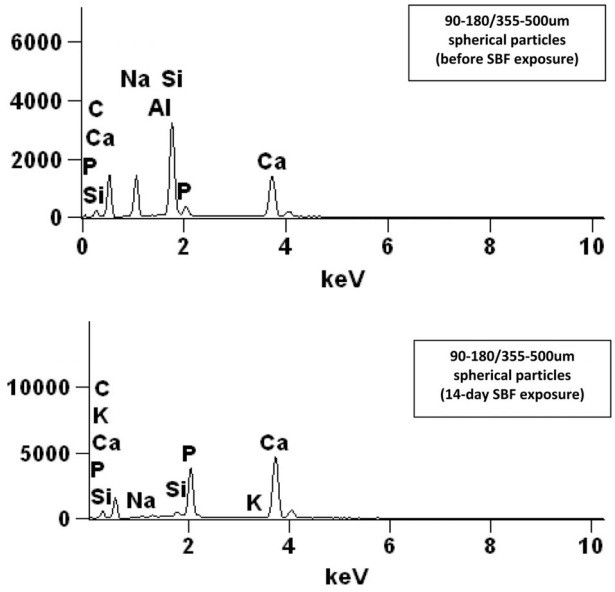

FIGURE 8 SEM-EDX spectra of the 90–180/355–500μm spherical particles (Group 4) before and after 14-day immersion in simulated body fluid; presence of a bioactive layer is indicated by the disappearance of the silicon (Si) peak in the pre-immersion spectra (top) and appearance of a phosphorus (P) peak in the post-immersion spectra (bottom)

4 | DISCUSSION

Over several decades, continued research on use of bioactive glass as a bone graft material has led to a more complete understanding of how the glass behaves in a physiological environment and how it can positively influence the bone formation response. The core property driving these effects is the ability of the glass to slowly dissolve when exposed to water. Upon implantation, bioactive glass dissolution leads to the release of soluble ions derived from the glass composition. These ions drive the bioactivity response which results in the formation of a HCA layer on the surface of the glass. Early *in vivo* studies examining this effect showed that the bioactive layer enhanced the osteoconductive bone formation response and led to chemical bond between the glass and the newly formed bone.[11] In the 1990's, bioactive glass dissolution ions were also found to play a significant role in the cellular healing response.[10] The discovery of this osteostimulatory property and the associated ionic effects on cells resulted in a shift in how bioactive glass was perceived and used as a bone graft material.[28,29] With this new data and understanding of the core mechanism of action, it became clear that the primary bone formation capacity of

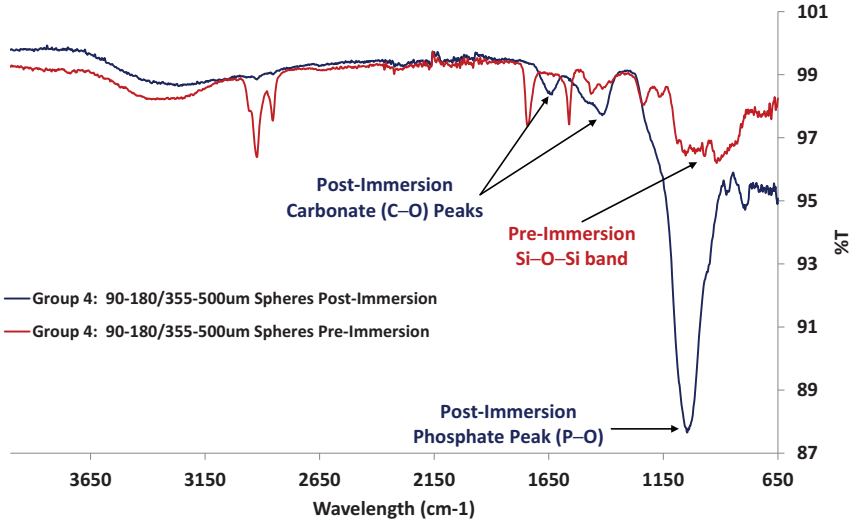

FIGURE 9 FTIR spectra of the 90–180/355–500μm spherical particles (Group 4) before and after 14-day immersion in simulated body fluid; presence of a bioactive layer is indicated by the appearance of distinct carbonate and phosphate peaks in the post-immersion spectra (blue line)

bioactive glass was being driven by local cellular osteostimulation which was additionally supported by its long-established bioactivity property. This mechanistic clarity fostered wider (and continued) adoption and use of bioactive glass products clinically. However, it was not until several years ago that this refined scientific understanding was strategically applied to bioactive glass material and product design to optimize the bone formation response.

In this study, a specifically designed spherical particle shape was chosen to provide greater control over the ionic properties of bioactive glass and its ability to support bone in-growth in the interparticle space. Preliminary chemical and physical characterization methods showed that the bioactive glass spheroidization process was effective in producing spherical particles with a uniform geometry and size. Following sphere fabrication, spheres of specific sizes could be easily isolated through simple sieving techniques. This allowed for the isolation of various unimodal size ranges and the ability to create specifically formulated bimodal size range combinations. Chemical characterization via XRF and XRD confirmed the 45S5 glass formulation was maintained and demonstrated that the melt-based spheroidization process did not alter the glass chemistry or crystallinity. Importantly, this characterization work showed that the spherical particle shape allowed for direct control over two critical bioactive glass bone formation parameters: particle packing and ion release.

The importance of particle packing has often been overlooked with bioactive glass bone graft products. Due to the lack of porosity within the typical, melt-derived bioactive glass particles, the interparticle spacing dictates the initial area available for bone in-growth. In moldable, putty-based graft materials, this space is initially occupied by the carrier. However, once the putty is implanted and the carrier is resorbed, the interparticle space becomes accessible for bone in-growth. Since bone regeneration at the bioactive glass implant site is ultimately governed by interparticle spacing, particle shape and size play a critical role in the speed and degree that new bone can form within the graft. As seen from the microCT image data, the spherical particle shape resulted in an open packing configuration that is immediately available to support bone in-growth throughout the graft area once the carrier is resorbed. The use of spherical particles provides for consistent, geometrically open space between the particles that allows for control over the bone ingrowth process though the particle matrix. Additionally, the three-dimensional arrangement of spherical particles also provides a stable and non-compressible architectural graft matrix that will not settle or lose overall volume. Conversely, particles with a flat surface and irregular geometry were characterized by denser packing patterns in the microCT imaging. Clinically, this reduced interparticle spacing may decrease or delay the ability of an irregular particle graft to support the initial bone in-growth response. With this type of particle packing, additional in-growth would be dependent on the complete resorption of smaller particles in order to open up more interparticle space.

In addition to interparticle spacing, this study showed that the shape and size of bioactive glass particles are also related to the dissolution process and resultant ion release. By using a spherical shape and controlling size, spherical particles can provide direct material control over the ion release kinetics, and ion-based properties (bioactivity and cellular osteostimulation). This is due to the uniform diffusion distance within a spherical particle and tighter control over spherical particle surface area. In the ion release portion of this study, bioactive glass particles of varying shape and size ranges were immersed in simulated body fluid for 14-days to examine silicon ion release and bioactivity. These samples were compared against a commercially available bioactive glass particles with an irregular shape, and broad, bimodal size range (32–125/90–710 μm). Silicon release profiles measured by ICP confirmed the expectation that bioactive glass dissolution was controlled by particle shape and size. Smaller spherical particles with a higher surface area had a greater exposure to the surrounding SBF solution. In these particles, the dissolution process progressed faster, which resulted in higher silicon ion concentrations. Additionally, during the first 10-h of exposure, all samples demonstrated a burst release of silicon. The burst effect was attributed to the release of ions close to the surface of the bioactive glass particles. Once these regions were depleted, the release profile transitioned to a relatively uniform release rate that lasted the remainder of the 14-day study. Comparing the spherical groups, the smallest sphere group (90–180 μm) showed the fastest release and highest cumulative silicon amounts. The 180–355 μm group showed a moderate release while the largest 355–500 μm sphere showed the slowest release. The spherical bimodal groups fell within these fast and slow profiles. With the exception of the 90–180 μm sphere group, the spherical particle profiles stayed relatively uniform throughout the duration of the SBF exposure. This showed that the uniform spherical shape and narrow size ranges could result in consistent dissolution profiles. The irregular particle group showed a different dissolution profile that initially started as the fastest release profile for the first 60-h, and then transitioned to a slightly slower release (marginally under the 90–180 μm group) for the remainder of the 14-day exposure. This was attributed to the larger number of small particles in the broad size range (32–710 μm) seen in the particle size analysis.

At the end of the 14-day ion release study, SBF-exposed samples were also characterized for the presence of a bioactive layer. Surface characterization data via SEM–EDX and FTIR were compared to unexposed controls to evaluate the change in surface appearance and chemistry. The characterization data confirmed that the bioactive layer consistently formed on all particles regardless of shape of size. FTIR analysis of the particles prior to SBF exposure showed a typical Si—O—Si band that is characteristic to bioactive glass. After SBF exposure, this disappeared from the FTIR spectra and was replaced by a strong phosphate peak (P—O) and carbonate peak (C—O). The presence of carbonate peak similar to the FTIR spectra of bone[27] confirmed that the bioactive layer was composed of carbonated apatite (HCA). This was additionally corroborated by the SEM–EDX data which showed an increase in calcium and phosphorus content in the post-immersion samples and an absence of silicon (which was seen on the pre-immersion samples). Visually, SEM imaging showed the presence of HCA coating over the surface of the all the particles. The results were attributed to the 45S5 composition of all of the samples

(confirmed by XRF and XRD) and the well-establish bioactivity property of 45S5 bioactive glass.

Overall, the data showed that spherical particles of bioactive glass could be effectively produced with uniform spherical shape and an accurate size range. The spheroidization process maintained the 45S5 glass composition and chemistry. Exposure to SBF showed that particle shape and size directly affected silicon ion release. The bioactivity response at 14 days appeared to be consistent across all groups. Although the bioactivity study did not show a difference between the groups, only a single 14-day characterization was done. Future testing can look at the bioactive response over time to determine if ion release rate affects the speed, in which the bioactive layer forms. Additionally, an *in vivo* bone defect study could evaluate the effect of sphere size and ion release on bone formation. This would be helpful in identifying which sphere size has the most optimal interparticle spacing and which ion release profile results in the best bone formation response.

5 | CONCLUSION

Bioactive glass dissolution and ion release impart unique and characteristic dual-mechanism effects on bone formation that is simultaneously osteostimulatory (primary effect) and bioactive (concurrent secondary effect). This combined mechanism is well-studied and established, but has only recognized a minimal application of purposeful biomaterial design to optimize the bone formation response. This study represents a pivotal investigation of differential bioactive glass particle geometry and size as strategic material characteristics that can optimize the bone formation pathway of this synthetic graft material. These properties are associated with the ability of the graft matrix to support interparticle bone in-growth and the potential for refined control of the ion-release process that occurs during dissolution. Based on the data, spherical particles have been shown to provide a uniform shape that maintains the chemical and bioactive properties of the starting 45S5 glass material. The sphere shape additionally allows for precise isolation of specific particle sizes. By using bioactive glass spheres in a bone graft putty form, the three-dimensional graft matrix consists of a regular and consistently open particle packing configuration that geometrically maintains an optimal interparticle space for bone in-growth. This represents a significant improvement on first-generation, irregular particle bioactive glass. Further work will examine the *in vivo* effects of particle shape and size on bone formation and a provide a more detailed view on the time-based formation of a bioactive layer.

ACKNOWLEDEMENTS

This study was financially supported by Synergy Biomedical, LLC.

CONFLICT OF INTEREST

The following authors report a financial interest and/or ownership in Synergy Biomedical: Mark Borden, William Walsh, and L. Erik Westerlund.

DATA AVAILABILITY STATEMENT

The data that support the findings of this study are available from the corresponding author upon reasonable request.

REFERENCES

1. Hench LL, Splinter RJ, Allen WC, Greenlee TK. Bonding mechanisms at the interface of ceramic prosthetic materials. *J Biomed Mater Res*. 1971;5:117-141. doi:10.1002/jbm.820050611
2. Hench LL, Paschall HA. Direct chemical bond of bioactive glass-ceramic materials to bone and muscle. *J Biomed Mater Res*. 1973;7:25-42. doi:10.1002/jbm.820070304
3. Clark AE, Hench LL, Paschall HA. The influence of surface chemistry on implant interface histology: a theoretical basis for implant materials selection. *J Biomed Mater Res*. 1976;10:161-174. doi:10.1002/jbm.820100202
4. Kokubo T. Bioactive glass ceramics: properties and applications. *Biomaterials*. 1991;12:155-163. doi:10.1016/0142-9612(91)90194-F
5. Kokubo T, Kushitani H, Ohtsuki C, Sakka S, Yamamuro T. Effects of ions dissolved from bioactive glass-ceramic on surface apatite formation. *J Mater Sci Mater Med*. 1993;4:1-4. doi:10.1007/BF00122969
6. Hench LL. Bioceramics: from concept to clinic. *J Am Ceram Soc*. 1991;24:1487-1510.
7. Lin F-H, Yao C-H, Huang C-W, Liu H-C, Sun J-S, Wang C-Y. The bonding behavior of DP-bioglass and bone tissue. *Mater Chem Phys*. 1996;46:36-42. doi:10.1016/0254-0584(96)80127-1
8. Hayashi K, Kishida R, Tsuchiya A, Ishikawa K. Honeycomb blocks composed of carbonate apatite, β-tricalcium phosphate, and hydroxyapatite for bone regeneration: effects of composition on biological responses. *Mater Today Bio*. 2019;4:100031. doi:10.1016/j.mtbio.2019.100031
9. Patel N, Gibson IR, Hing KA, et al. The in vivo response of phase pure hydroxyapatite and carbonate substituted hydroxyapatite granules of varying size ranges. *Key Eng Mater*. 2001;218–220:383-386. www.scientific.net/KEM.218-220.383
10. Wilson J, Low SB. Bioactive ceramics for periodontal treatment: comparative studies in the patus monkey. *J Appl Biomater*. 1992;3:123-129. doi:10.1002/jab.770030208
11. Fujishiro Y, Hench LL, Oonishi H. Quantitative rates of in vivo bone generation for bioglass® and hydroxyapatite particles as bone graft substitute. *J Mater Sci Mater Med*. 1997;8(11):649-652.
12. Xynos ID, Edgar AJ, Buttery LDK, Hench LL, Polak JM. Gene-expression profiling of human osteoblasts following treatment with the ionic products of bioglass® 45S5 dissolution. *J Biomed Mater Res*. 2001;55(2):151-157.
13. Xynos ID, Hukkanen MVJ, Batten JJ, Buttery LD, Hench LL, Polak JM. Bioglass® 45S5 stimulates osteoblast turnover and enhances bone formation in vitro: implications and applications for bone tissue engineering. *Calcif Tissue Int*. 2000;67:321-329. doi:10.1007/s002230001134
14. Xynos ID, Edgar AJ, Buttery LDK, Hench LL, Polak JM. Ionic products of bioactive glass dissolution increase proliferation of human osteoblasts and induce insulin-like growth factor II mRNA expression and protein synthesis. *Biochem Biophys Res Commun*. 2000;276:461-465. doi:10.1006/bbrc.2000.3503
15. Yong-cheng H, Ji-pin Z. Osteostimulation of bioglass. *Chin Med J*. 2009;122(19):2386-2389.
16. Bosetti M, Cannas M. The effect of bioactive glasses on bone marrow stromal cells differentiation. *Biomaterials*. 2005;26:3873-3879. doi:10.1016/j.biomaterials.2004.09.059
17. Jell G, Notingher I, Tsigkou O, et al. Bioactive glass-induced osteoblast differentiation: a noninvasive spectroscopic study. *J Biomed Mater Res*. 2008;86A:31-40. doi:10.1002/jbm.a.31542
18. Bielby RC, Pryce RS, Hench LL, Polak JM. Enhanced derivation of osteogenic cells from murine embryonic stem cells after treatment

with ionic dissolution products of 58S bioactive sol–gel glass. *Tissue Eng*. 2005;11:479-488. doi:10.1089/ten.2005.11.479
19. Day RM. Bioactive glass stimulates the secretion of angiogenic growth factors and Angiogenesisin vitro. *Tissue Eng*. 2005;11:768-777.
20. Gorustovich AA, Boccaccini AR. Effect of bioactive glasses on angiogenesis: a review of in vitro and in vivo evidences. *Tissue Eng Part B Rev*. 2010;16(2):199-207.
21. Leu A, Stieger SM, Dayton P, Ferrara KW, Leach JK. Angiogenic response to bioactive glass promotes bone healing in an irradiated calvarial defect. *Tissue Eng Part A*. 2009;15:877-885. doi:10.1089/ten.tea.2008.0018
22. Jones JR. Review of bioactive glass: from Hench to hybrids. *Acta Biomater*. 2013;9:4457-4486. doi:10.1016/j.actbio.2012.08.023
23. Radin S, Ducheyne P. Effect of serum proteins on solution-induced surface transformationsbf bioactive ceramics. 1996;30(3):273-279.
24. Bhakta S, Pattanayak DK, Takadama H, et al. Prediction of osteoconductive activity of modified potassium fluorrichterite glass-ceramics by immersion in simulated body fluid. *J Mater Sci*. 2010;10:2979-2988.
25. Rezaei Y, Moztarzadeh F, Shahabi S, Tahriri M. Synthesis, characterization, and *in vitro* bioactivity of sol-gel-derived SiO_2–CaO–P_2O_5–MgO-SrO bioactive glass, synthesis and reactivity in inorganic, metal-organic, and nano-metal. *Chemistry*. 2014;44:692-701. doi:10.1080/15533174.2013.783869
26. Notingher I, Jones JR, Verrier S, et al. Application of FTIR and Raman spectroscopy to characterisation of bioactive materials and living cells. *Spectroscopy*. 2003;17:275-288. doi:10.1155/2003/893584
27. Ren FZ, Leng Y. Carbonated apatite, type-A or type-B? *Key Eng Mater*. 2011;493–494:293-297. www.scientific.net/KEM.493-494.293
28. Hench LL. The story of bioglass®. *J Mater Sci Mater Med*. 2006;17:967-978. doi:10.1007/s10856-006-0432-z
29. Hench LL. Chronology of bioactive glass development and clinical applications. *N J Glass Ceram*. 2013;3:67-73. doi:10.4236/njgc.2013.32011

How to cite this article: Borden M, Westerlund LE, Lovric V, Walsh W. Controlling the bone regeneration properties of bioactive glass: Effect of particle shape and size. *J Biomed Mater Res*. 2022;110(4):910-922. doi:10.1002/jbm.b.34971